J. Fluid Mech. (1987), *vol.* 176, *pp.* 169–190
Printed in Great Britain

Coastal upwelling on a sloping bottom: the formation of plumes, jets and pinched-off cyclones

By S. NARIMOUSA AND T. MAXWORTHY†
Department of Mechanical Engineering, University of Southern California, Los Angeles, CA 90089-1453, USA

(Received 7 July 1986)

An experimental, two-layer, stratified model of coastal upwelling was produced at the outer edge of a cylindrical tank having a conical bottom. As in Narimousa & Maxworthy (1985), we find that most of the characteristics of the flow field can be described by the single non-dimensional parameter $\theta_* = g'h_0/u_* f\lambda_s$ (where $g' = g\delta\rho$ is the reduced gravity, h_0 is the initial depth of the top layer, u_* is the friction velocity applied to the top surface of the fluid, f is the Coriolis parameter and λ_s is the distance of the stationary position of the upwelling front at the surface from the wall of the tank). For example, we find that the migration rate of the front at the surface, u_f is given by $u_f/u_* \sim \theta_*^{-\frac{1}{2}}$; the size λ_w of the frontal, circular waves is $\lambda_w/\lambda_s \sim \theta_*$; that these waves first appear at the front when it has moved a distance $\lambda_i < \lambda_s$ given by $\lambda_i/\lambda_s \sim \theta_*^{-\frac{1}{2}}$; and have a final drift velocity $u_w \approx 0.5\,U$ in the direction of the applied stress (where U is the mean velocity of the top layer). At low values of θ_* complex interactions between the growing waves created intense meandering jets which transported upwelled fluid far from the mean position of the front.

1. Introduction

Owing to the important role played by coastal upwelling in marine life, fisheries, climatology, oil slick dispersion, waste material disposal, offshore oil drilling, etc. it has become one of the most studied problems in oceanography, ocean and civil engineering. The west coasts of North America (Mooers, Collins & Smith 1976; Halpern 1976), South America (Brink *et al.* 1981) and West Africa (Halpern 1977) are among the most active regions of coastal upwelling in the world. In these examples, an equatorward, alongshore wind stress causes the warmer surface water to drift away from the coast and allows cold, nutrient-rich, bottom water to upwell and appear in a narrow band at the surface near the coast. The two masses of cold and warm water are separated by a sharp front which continues to migrate offshore. During its migration, the front becomes unstable to wave-like disturbances (§5) and, as seen in many satellite infrared images, filaments and plumes of cold water propagate far offshore from the front (Flament, Armi & Washburn 1985; Breaker & Mooers 1985). Such instabilities could be triggered by interaction with a coastline perturbation, bottom topography, a field of offshore eddies or by a shear instability of the front itself (Narimousa & Maxworthy 1986*a*). It is the objective of our continuing study to understand the role of each of the above-mentioned effects on the evolution and dynamics of coastal currents and fronts leading to the generation of eddies that can then separate or pinch-off from the front and jets of upwelled fluid that penetrate

† Also Department of Aerospace Engineering, USC and Earth & Space Sciences Division, J.P.L., Pasadena, CA, USA.

far offshore. Each of the effects has been considered, independently, in separate series of experiments in order to try to understand the role of each of them in generating the observed features. Thus in Narimousa & Maxworthy (1985, hereinafter referred to as NM1) and Maxworthy & Narimousa (1985) we studied the role of bottom topography in creating energetic offshore jets (see also Preller & O'Brien 1980) and compared the results to the observations of Brink *et al.* (1980), Breaker & Mooers (1985) and Mooers & Robinson (1984). The effect of a field of offshore eddies generated by a curl of the wind stress has been reported in Narimousa & Maxworthy (1986*b*) and again comparison with some features of the observed flows off of the west coast of North America (Simpson, Dickey & Koblinsky 1984; Bernstein, Breaker & Whirtner 1977; and Huyer, Smith & Hickey 1984, among others), was encouraging.

In the present experiments, we study coastal upwelling on a sloping bottom, free of bottom topographic features and coastline perturbations, which, although it could be thought of as the first and simplest of this series of experiments, has been delayed because of the clear, critical importance of the aforementioned effects on coastal upwelling. However, the present study is important in its own right, because there are situations in which the coastal upwelling circulation is free of the effects of the significant bottom and coastline perturbations. Under these conditions, according to satellite infrared images, offshore filaments of cold water and pinched-off eddies can occur also.

The instability of such a front in a rotating environment has been discussed by Eady (1949), Phillips (1954), Hide (1971), Hart (1972, 1980), Douglas, Hide & Mason (1972), Saunders (1973), and Griffiths & Linden (1981*a*, *b*) among others. In these descriptions, the normalized Rossby deformation radius was used as a control parameter, and there was general agreement that when this parameter was less than about unity, baroclinic waves should appear at the density front. The study of NM1 indicated that in a flow where the velocities across the front were not given *a priori* and the flow was driven by a surface shear stress there is probably another parameter, θ_* which determines the occurrence of such instabilities. The parameter $\theta_* = g'h_0/u_* f\lambda_s \equiv Ri_*^{\frac{1}{2}}\theta$, where $Ri_* = g'h_0/u_*^2$ is the Richardson number and $\theta = (g'h_0)^{\frac{1}{2}}/f\lambda_s$ is the dimensionless Rossby deformation radius. In the present study we have overcome some of the difficulties described in NM1, and have conducted our experiments in an extended range of values $120 \leqslant Ri_* \leqslant 750$, $0.085 \leqslant \theta \leqslant 2.3$ and $0.9 \leqslant \theta_* \leqslant 38$. Such a large variation in the values of Ri_*, θ and θ_*, compared with those of NM1, have enabled us to choose what we believe is the right non-dimensional parameter for prediction of the appearance of baroclinic waves (see §5). In §5 we also present measurements of the migration rate of the upwelled front, the size of the eddies, their drift velocity, and a comparison with similar results from NM1 and experiments of Saunders (1973), Griffiths & Linden (1981*a*, *b*, 1982) and Chia, Griffiths & Linden (1982) and theories of Phillips (1954) and Killworth, Paldor & Stren (1984).

2. The experiments

The present experiments were conducted in the same apparatus as that of NM1, but with the bottom topography (ridge) removed. For a detailed discussion the reader is referred to NM1; only a brief description will be given here.

Two layers of salt water of slightly different densities were brought to solid-body, counter-clockwise rotation inside a cylindrical tank (90 cm in diameter and 22 cm in depth) having a conical bottom with a slope of 0.27 (figure 1). The top layer was in

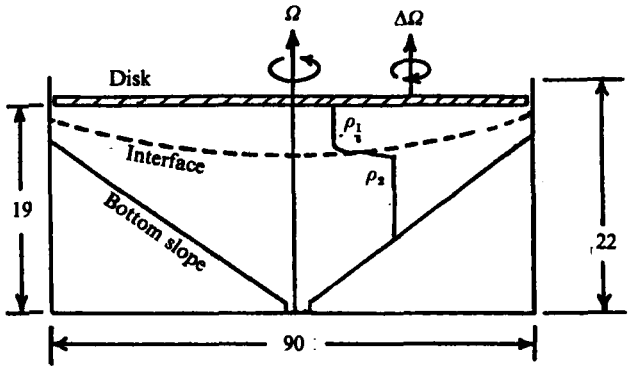

FIGURE 1. Cross-sectional side view of the experimental tank, with a conical bottom of 0.27 slope. Lengths in cm.

contact with a rotating, circular, smooth disk, so that a stress was applied to this layer, in analogy to the wind stress at the air–sea interface. For the purposes of this study the disk was rotated in a clockwise direction, opposite to that of the main tank. This in turn produced an upwelling around the outer edge of the tank, allowing bottom-layer fluid to appear at the surface as the upwelled front migrated outward. The front at some point became unstable and baroclinic waves appeared. In order to observe this frontal movement and reveal the structure of the circular waves, small neutrally buoyant particles were placed in the interface between the two layers and their motions recorded by streak photography. The direction of motion of these particles was found by firing an electronic flash at the beginning of the time exposure. In order to reveal the structure of the circular waves either the camera was rotated a rate almost equal to the speed of wave propagation, or a white, liquid-titanium dye was introduced at the wall near the surface of the bottom-upwelled water. The density of the dye was lower than that of both layers and so remained near the surface to reveal the flow activities within the bottom-upwelled water near the surface. When dye was released near the wall it was advected downstream by the mean flow, while at the same time it drifted offshore due to the Ekman-layer flow. As a result when the dye eventually reached the front at some distance downstream from its origin it revealed the wave activities at the front and was also transported offshore by the jets that were produced by the interaction of the vortex structures generated at the front (see §6).

The present study employed the same method as that of NM1 based on experiments of Narimousa, Long & Kitaigorodskii (1985) to estimate the disk friction velocity u_* at the location of the stationary front at the surface. According to Narimousa *et al.* (1985) the mean velocity in the upper layer $U = 10.6u_*$. In NM1 we found that $U = 0.74U_p$ (U_p is the disk velocity and U the velocity of the top layer measured from streak photography) and estimated $u_* = 0.07U_p$ (with an error of about 10–15%), which is in good agreement with measurements by Kantha, Phillips & Azad (1977) (for details see NM1).

In the present experiments, the parameters took the following values: initial depth of the top layer $1.35 \leqslant h_0 \leqslant 2.8$ cm; density difference between the two layers $0.016 \leqslant \delta\rho_0 \leqslant 0.059$ g cm^3 ($\delta\rho_0 = \rho_2 - \rho_1$); reduced gravity between the two layers $39 \leqslant g' \leqslant 133$ cm s^{-2} ($g' = g\delta\rho_0$), where $g = 981$ cm s^{-2} is the acceleration due to gravity; the Coriolis parameter $0.924 \leqslant f \leqslant 5.46$ rad s^{-1}; the friction velocity $0.28 \leqslant u_* \leqslant 0.62$ cm s^{-1} so that θ_* varied within the range $0.9 \leqslant \theta_* \leqslant 38$.

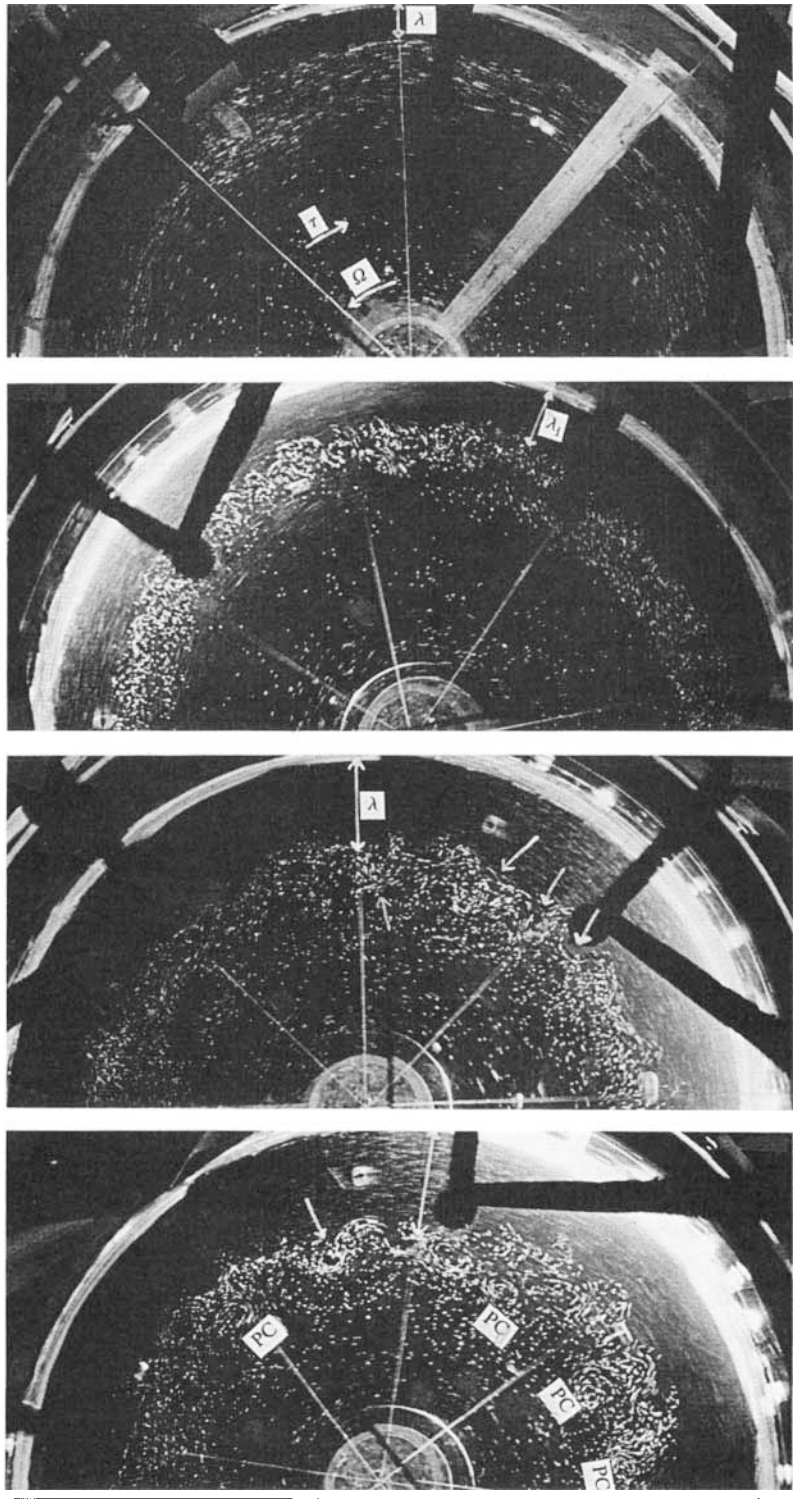

FIGURE 2. For caption see facing page.

3. Qualitative description of the flow field

After the two-layer fluid system was brought to solid-body rotation, at a rate Ω s^{-1}, the top disk was set to rotate anticyclonically, at rate $\Omega - \Delta\Omega$ s^{-1}, thus applying a stress to the top surface of the lighter fluid. The resulting Ekman flux caused the top layer to spin down and the interface to rise near the wall and to descend at the centre of the tank. At a later time, the interface intersected the top disk and a surface front was formed. This front then migrated away from the wall and allowed bottom fluid to contact the disk in a narrow strip of width λ around the outer edge of the tank, until a steady state was reached ($\lambda = \lambda_s$), and the system was in geostrophic balance. Before the front became stationary, at some time when $\lambda = \lambda_1 < \lambda_s$ the axisymetric front became unstable to baroclinic waves. In figure 2 we show a set of plan-view streak photographs to demonstrate these observations. Similar observations were reported by NM1, in their description of the upwelled flow upstream of bottom topography.

In a given experiment, when baroclinic waves first appeared at the axisymmetric front they had a small wavelength, but they continued to grow until they reached a maximum size (see §5). These waves had a large azimuthal drift velocity (u_w) in the direction of the applied stress. At the beginning, the wave velocity was small, but continued to increase as the wavelength grew, until it reached its final velocity and size. We find that the wave velocity in the present experiment is considerably greater than that of the waves observed upstream of the bottom topography in NM1, while it is smaller by about 20% than those measured in some preliminary, unpublished, experiments in a deep tank with no sloping bottom (see §5).

When the axisymmetric front became unstable, a meandering, jet-like wave motion was produced around the outer edge of the upwelled front, with cyclones to the offshore side (at a wave trough) and anticyclones to the inshore side (at a wave crest) (see figure 2). At small values of θ_*, as a result of the growth of a large-amplitude frontal instability, the wave troughs took the form of a plume with a narrow middle and enlarged head. A few rotation periods later the head of this plume was pinched-off to form a circular cyclone containing bottom fluid which interacted with a neighbouring frontal anticyclone to produce an outward meandering jet-like motion. At moderate values of θ_* the troughs sometimes grew in amplitude but unlike those at low values of θ_*, these troughs propagated in the alongshore direction (see figure 3). Eventually cyclones were pinched-off from the head of these alongshore-propagating plumes. These cyclones also interacted with a frontal anticyclone to also produce outward meandering jet-like motion (see figure 3).

FIGURE 2. A set of streak photographs with a 0.5 s time exposure and with parameter values of $\Omega = 2.77$ rad s^{-1}, $\Delta\Omega = 0.185$ rad s^{-1}, $h_0 = 2.6$ cm, $\delta\rho = 0.018$ g cm^{-3}, $u_* = 0.36$ cm s^{-1} (estimated at the location of the stationary front), $\lambda_s = 17$ cm, and $\theta_* = g'h_0/u_* f\lambda_s = 1.68$ ($g' = g\delta\rho_0$). In these photographs the region around the outer edge of the tank, with no particles, indicates the width of the bottom upwelled flow (λ) at the surface. (*a*) was taken at $t = 22$ s, the camera was stationary in the rotating frame of the turntable, and the upwelled front is axisymetric with no waves. (*b*) was taken at $t = 105$ s. Here the camera was rotating with a speed almost equal to the speed of the waves, which are just beginning to appear at the front when $\lambda = \lambda_1$. (*c*) was taken at $t = 320$ s and again the camera was rotating with the waves. Here the size of the frontal waves is greater than those of (*a*). On (*d*), taken at $t = 370$ s, we have marked plumes of bottom fluid by arrows and these may evolve into pinched-off cyclones. The camera was rotating with the waves and the front is close to its stationary position $\lambda \leqslant \lambda_s$. In (*d*) we observe a number of pinched-off cyclones (PC) containing bottom fluid, generated from the large amplitude instability of the plumes of photographs (*b* and *c*).

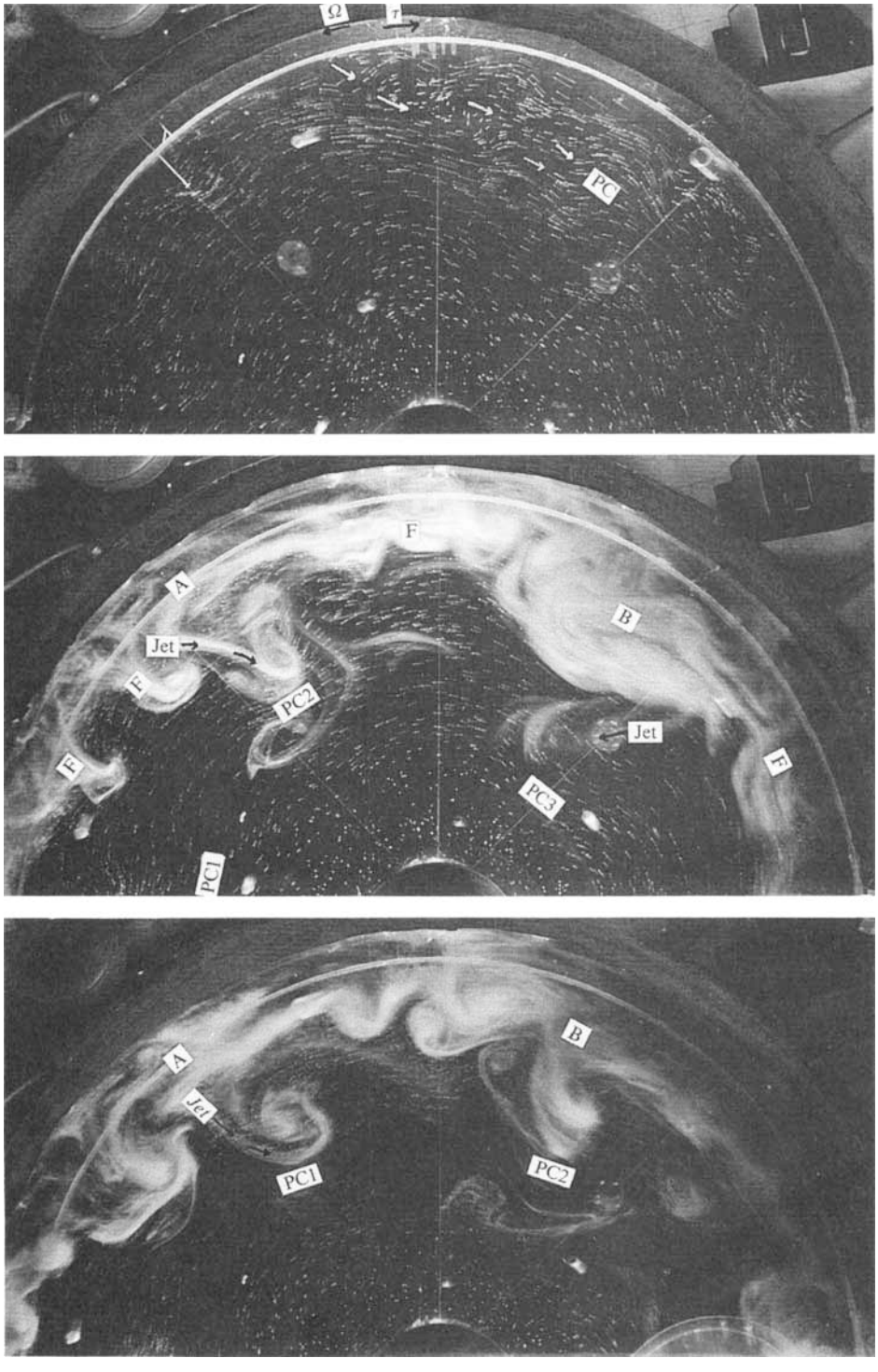

FIGURE 3. For caption see facing page.

The streak photographs clearly reveal the presence of offshore jets of upwelled fluid. To demonstrate further that these jets were responsible for offshore transport of bottom water either in the form of a pinched-off cyclone or an offshore jet, the upwelled bottom water was dyed by the method described in (§2). When dye interacted with the front, it not only revealed the structure of the baroclinic frontal waves, but it was also transported offshore by the jets and pinched-off eddies.

4. Theoretical discussion

In our first paper (NM1) we produced a simple theoretical model, similar to that of Linden & van Heijst (1984) (hereinafter LV) to estimate the final width of the bottom fluid at the surface (λ_s), and we found

$$\frac{\lambda_s}{R_0} = 1 - \left(\frac{g'h_0}{3.58 f U_* R_0}\right)^{\frac{1}{2}}, \tag{1}$$

where $U_* = 0.07 R_0 \Delta\Omega$ is the maximum friction velocity measured at the outer edge of the disk, and R_0 is the tank radius, and it was assumed that the top layer was rotating at the same rate as the plate. In terms of $\Theta = g'h_0/fU_* R_0$, (1) becomes

$$\frac{\lambda_s}{R_0} = 1 - 0.73\Theta^{\frac{1}{2}}. \tag{2}$$

Values of λ_s calculated from (1) were in good agreement with the measured values of λ_s in the experiments of NM1, upstream of their bottom topography. This is probably fortuitous since it was observed that the upper layer actually rotated at a somewhat slower rate than the plate. We suspected that the upstream blocking effect of the ridge compensated for this effect, which would tend to decrease λ_s, to give reasonable agreement with the measurements. In NM1 we used the calculated values of λ_s, as the appropriate length with which to scale the measurements in order to apply the experimental results to field measurements and observations. The measured values of the friction velocity at the location of stationary front, u_*, were used to define the parameter

$$\theta_* = \frac{g'h_0}{u_* f \lambda_s}. \tag{3}$$

This parameter θ_*, appeared to determine many of the dynamical features of the coastal-upwelling circulation.

FIGURE 3. A set of streak photographs where dye has also been injected, with a 0.5 s time exposure and parameter values of $\Omega = 1.48$ rad s^{-1}, $\Delta\Omega = 0.14$ rad s^{-1}, $h_0 = 2.65$ cm, $\delta\rho_0 = 0.026$ g cm^{-3}, $\lambda_s = 11.6$ cm, $u_* \approx 0.33$ cm s^{-1} and $\theta_* \approx 5.6$. Here the camera was stationary in the frame of the rotating tank. (*a*), taken after about a 150 rotation periods, shows well-developed baroclinic cyclonic and anticyclonic waves at the front, all around the tank. The alongshore propagation of the trough and the resultant pinched-off cyclone (PC) near the front is indicated. There is also another PC at the bottom left corner of (*a*). (*b*) was taken 30 rotation periods after (*a*). Here, beside particle streaks, dye has also been introduced into the bottom upwelled flow near the surface. In this photograph the dye has interacted with the upwelled front and some of the frontal waves are indicated by F. Notice the pinched-off cyclone (PC2) at A and the corresponding offshore jet which has transported the bottom, dyed water into the cyclone offshore to produce a mushroom type of vortex. There are also pinched-off cyclones PC1 at the bottom-left corner of (*b*) and at PC3 with the related offshore jet also clearly shown. (*c*) was taken 7 rotation periods after (*b*). The PC1 of photograph (*b*) has reached A, PC2 is now at B while PC3 has travelled out of the field of view of the camera. Here the dye trapped in PC1 reveals a cyclonic flow only.

The present study also uses θ_*, but with a slight change in the calculation of the values of λ_s. We should note that (1) was found based on the geostrophic balance

$$-f(U_p) = g' \frac{d\eta_s}{dr}, \tag{4}$$

where r is radial coordinate measured from the origin at the centre of the tank and η_s the depth of the front from the surface in steady state conditions. The measurements of NM1 indicated that $U = 0.74U_p$, a result that was also confirmed in measurements from the present study. In (4), we replaced U_p by this measured fluid velocity of the top layer, U, so that the balance equation becomes

$$-fU = g' \frac{d\eta_s}{dr}. \tag{5}$$

Solving (5) with the same method as that of NM1 or LV we find

$$\frac{\lambda_s}{R_0} = 1 - 0.66\theta_*^{\frac{1}{2}}. \tag{6}$$

We see that in comparison with (2), (6) gives smaller values of λ_s, which are in better agreement with those measured in the present study. These theoretical results (2), (6), and those of the experimental measurements suggest that bottom topography can cause the upstream front to migrate farther from the coast than in the present study and corroborates our feelings that the presence of the ridge disrupts the basic geostrophic balance used to obtain (2). In §5 we shall see that for smaller values of θ_* the difference between the calculated values of λ_s from (2) and (6) is within the experimental error of about 10 %, while at higher values of θ_* the difference is higher, indicating the strong effect of the bottom topography on the upstream front at higher values of θ_*.

When $\lambda_s = 0$, (6) reduces to

$$\theta_* = 5.27. \tag{7}$$

This condition implies that only when $g'h_0/fU_*R_0 < 5.27$, does the outer edge of the front migrate away from the wall and allow bottom fluid to appear at the surface in the absence of instability.

5. Quantitative results

5.1. *Front migration rate*

From photographs, like those shown in figure 2, we measured the average value of λ around the outer edge of the upwelled front at the surface, and plotted these values as a function of time t. The results of four experiments are shown in figure 4, and they indicate that the front initially migrated with a constant speed, $u_f = d\lambda/dt$, then slowed until, eventually, the Coriolis force and the radial pressure gradient caused by the front deformation balanced, and the front became stationary. In figure 4, the solid lines parallel to the time axis are the calculated values of λ_s from (6).

In order to obtain the dependence of the migration rate on the control parameters we plotted the dimensionless migration rate u_f/u_* against the values of θ_*, in figure 5, where the results are compared with those of NM1. It can be seen that for $\theta_* \leqslant 10$ the migration rates of NM1 are within the experimental error of the present study. For values of $\theta \geqslant 10$ the migration rates of NM1 are lower. Since, at the higher values of θ_*, the upwelling front did not migrate far from the wall of the tank, this suggests

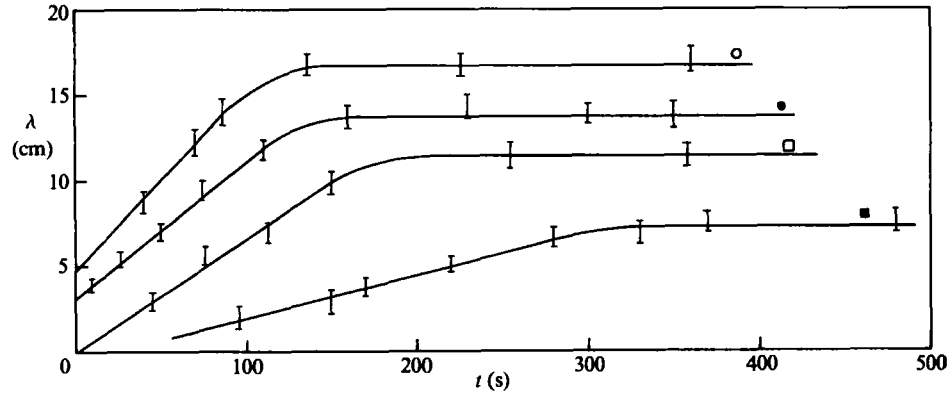

FIGURE 4. Variations of the width λ of the upwelled layer at the surface with time for various values of θ_*. The solid lines parallel to the t-axis are the calculated values of λ_s from (6) and the symbols represent:

	f rad s^{-1}	h_0 cm	$\delta\rho_0$ g cm^{-1}	u_* cm s^{-1}	λ_s cm	u_f cm s^{-1}	θ_*	t_{sm} s	t_{sc} s
○	1.7	1.4	0.02	0.54	16.7	0.11	1.8	110	60
●	3.98	2.07	0.045	0.6	13.7	0.084	2.8	130	115
□	1.68	2.6	0.02	0.61	11.4	0.067	4.37	170	105
■	2.42	2.55	0.019	0.28	7.21	0.026	9.8	310	276

where t_{sm} is the measured values of t_s from (10) and t_{sc} are calculated values of t_s from the criterion presented in LV.

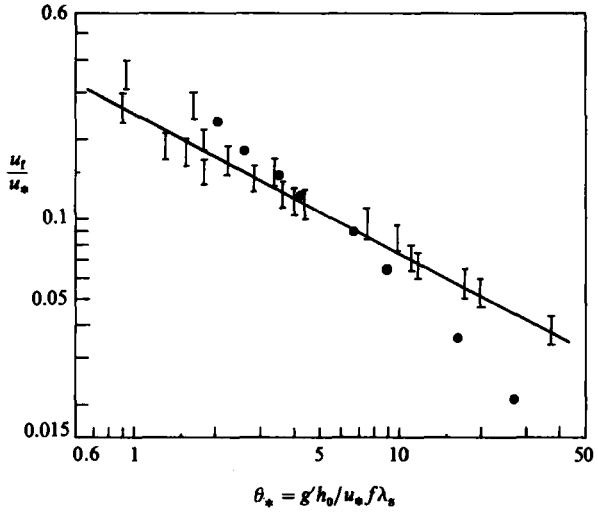

FIGURE 5. The variation of migration rate of the front at the surface u_f/u_* with θ_* (8). The dots are the average values of the migration rates taken from NM1.

that bottom topography had a considerable blocking effect on the upstream front in the experiments of NM1 which reduced its speed of migration.

In the present study instead of plate velocity U_p we use the measured mean fluid velocity to calculate λ_s from the geostrophic balance. This means that the theoretical values of λ_s for the present study are lower than those of NM1, and in agreement with the experimental results. For low values of θ_* (i.e. $\theta_* \leqslant 10$) the differences between the calculated values of λ_s from (2) and (6) is about 10 % and becomes lower

as the value of θ_* decreases. This suggests that for values of $\theta_* \leqslant 10$ whether one uses (2) or (6) in calculating the values of λ_s will not have a significant effect on the migration rate (see figure 5).

According to figure (5), we can write

$$\frac{u_f}{u_*} \approx 0.35\theta_*^{-\frac{1}{2}}. \tag{8}$$

Solving (8) for λ we find

$$\lambda = 0.35\theta_*^{-\frac{1}{2}} u_* t, \tag{9}$$

which estimates the linear dependence of λ as a function of time t. At steady state, $\lambda = \lambda_s$, and (9) becomes

$$t_s \approx 3.1 \left(\frac{\lambda_s}{u_* f}\right)^{\frac{1}{2}} Ri_*^{\frac{1}{2}} \equiv 3.1 \left(\frac{\lambda_s g' h_0}{u_*^3 f}\right)^{\frac{1}{2}}, \tag{10}$$

which gives the time t_s to reach a steady state.

The theoretical criterion for the spin-up time $t_s = (h_0/\Delta f)\,(2(f+\Delta f)/\nu)^{\frac{1}{2}}$ was found by LV, (where $\Delta f = 2\Delta\Omega$ and ν is the kinematic viscosity). Here we compared our measured values of t_s with those calculated from the LV criterion (see the table in the caption to figure 4). We found for those experiments with values of $\Delta f/f \leqslant 0.15$ that the LV criterion gave a good estimate of the values of t_s for our experiments, while as the values of $\Delta f/f$ increased above 0.15 the calculated values of t_s from the LV criterion were different by as much as 45 % from our measurements.

5.2 *A condition for the appearance of baroclinic waves*

One of our goals in the present study was to conduct more experiments in a range of values of θ_* much greater than those of NM1 in order to enable us to choose the most suitable and accurate condition for prediction of the occurrence of frontal instability. In figure 6 we show the plots of λ_1/λ_s as function of θ_* for 21 experiments in which we have been able to detect the first appearance of the waves, with reasonable accuracy. According to figure 6 we can write

$$\frac{\lambda_1}{\lambda_s} \approx 0.7\theta_*^{-\frac{1}{2}}. \tag{11}$$

We also made plots of λ_1/λ_s as a function of non-dimensional Rossby deformation radius and found that these contained considerably more scatter than those shown on figure 6. According to the present results, it seems that in stress-driven buoyancy currents, θ_* is the correct non-dimensional parameter with which to predict the appearance of the waves at the upwelling front. In previous experiments (Saunders 1973; Griffiths & Linden 1981*a*, *b*, 1982; Chia *et al.* 1982) where the stability of a similar type of front was considered, the fluid velocity was related to other independent parameters of the problem, e.g. the density difference, rotation rate, etc. In these cases the non-dimensional Rossby deformation radius $\theta_0 = (g' h_2)^{\frac{1}{2}}/fR_0$ (where R_0 is the cylinder radius) was considered as a control parameter, and the potential energy contained in the density field was the source of kinetic energy for the baroclinic instabilities. There is no doubt that the Rossby deformation radius plays a significant role in the evolution of such instabilities. In the present work, where the distorted density field is set-up by the application of a surface stress its magnitude should also appear in the formulation. Thus the appearance of θ and R_* together should not be surprising since one determines the instability of the front while the other measures the intensity of the forcing.

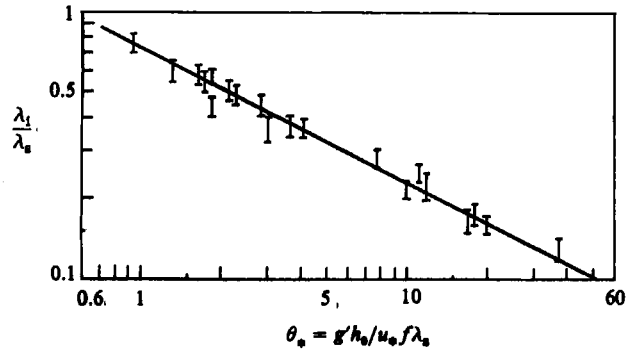

FIGURE 6. The variation of λ_1/λ_s with θ_*, where λ_1 is the front location when the waves first appear at the front.

5.3. *Size of the equilibrium baroclinic waves*

When waves first appeared at the front at a distance $\lambda_1 \leqslant \lambda_s$, they had their smallest wavelength. As time progressed neighbouring waves combined to create larger waves, a process that continued until the waves reached their 'saturated' size λ_w. To classify the final size of the waves λ_w we measured the average diameter of a frontal cyclone or anticyclone from photographs like figure 7. We then made a plots of λ_w/λ_s as a function of θ_*, with the results shown on figure 8. Here we present also the average of the data taken from NM1's plots of this same quantity.

According to figure 8 we can write

$$\frac{\lambda_w}{\lambda_s} \approx 0.15\theta_* \tag{12}$$

or

$$\theta_w = \frac{g'h_0}{u_* f\lambda_w} \approx 7, \tag{13}$$

indicating that size of the waves is independent of the final width of the upwelled flow at the surface (λ_s), and is in a reasonably good agreement with the values reported by Griffiths & Linden (1982) (hereinafter GL). To further investigate this agreement, we chose an experiment in which the front was far from the wall, so that similarity to GL experiments was achieved. In this particular experiment (see also §5.2) the parameters were $f = 4.46$ rad s^{-1}, $\lambda = 18.6$ cm, $h_0 = 2.8$ cm, $g' = 17.7$ cm s^{-2}, the total depth at location of the front was $H = 8.7$ cm, the mean depth of the top layer was $\bar{h} = R_0 h_0/R_0 - \lambda_s \approx 4.77$ cm and $L_w = 11.5$ cm. In GL a quantity $\hat{R} = \bar{R}(H/\bar{h} - 1)$ was defined, where $\bar{R} = (g'h_0)^{\frac{1}{2}}/f (= 1.93$ in our case) was the Rossby radius of the upper layer based on its mean depth $\bar{h}$. We find that $\hat{R} \approx 1.6$ and $L_w/2\pi\hat{R} = 1.14$, which for this latter quantity is in very good agreement with results from GL which gave 1.1 ± 0.3, Phillips (1954) which gave 1.08, Killworth *et al.* (1984) which gave 1.15 and Chia *et al.* (1982) which gave 1.16 ± 0.27.

Occasionally, at some point along the front, a wave grew to a size greater than the saturated value, at the expense of neighbouring waves which were reduced to a magnitude smaller than this value. This was not a permanent condition, however, and it occurred only occasionally and randomly, with the waves tending to remain close to their saturated values most of the time.

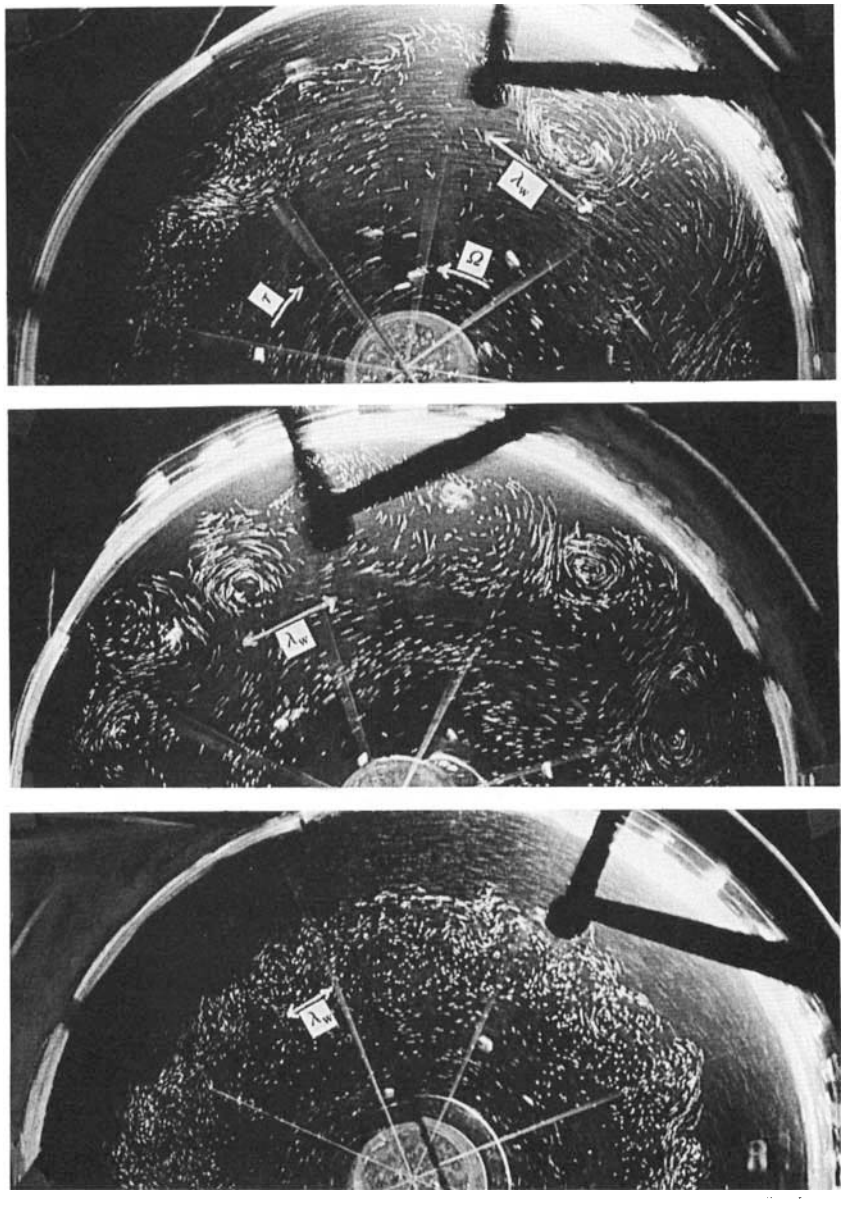

FIGURE 7. A set of streak photographs showing that the size of the waves λ_w decreases as the value of θ_* decreases. (*a*) has parameter values of $\Omega = 0.85$ rad s^{-1}, $\Delta\Omega = 0.114$ rad s^{-1}, $h_0 = 2.35$ cm, $\delta\rho_0 = 0.021$ g cm^{-3}, $u_* \approx 0.32$ cm s^{-1} and $\lambda_s = 4.44$ cm. In this experiment $\theta_* = 20$, and the size of the waves $\lambda_w \approx 15$ cm. (*b*) has parameter values of $\Omega = 0.97$ rad s^{-1}, $\Delta\Omega = 0.13$ rad s^{-1}, $h_0 = 2.55$ cm, $\delta\rho_0 =$ g cm^{-3}, $u_* \approx 0.35$ cm s^{-1} and $\lambda_s = 6.7$ cm. In this experiment the value of $\theta_* = 11$, and the size of the waves $\lambda_w \approx 12$ cm. The parameter values for (*c*) are as for figure 2 where the value of $\theta_* \approx 1.68$ and size of the waves $\lambda_w \approx 5$ cm. Note that u_* is measured at the stationary front and the camera was rotating with a speed close to that of the waves. In (*a*) and (*b*) the time exposure was 1 s, while for (*c*) it was 0.5 s. The directions of Ω and the applied stress τ for all photographs are shown in (*a*).

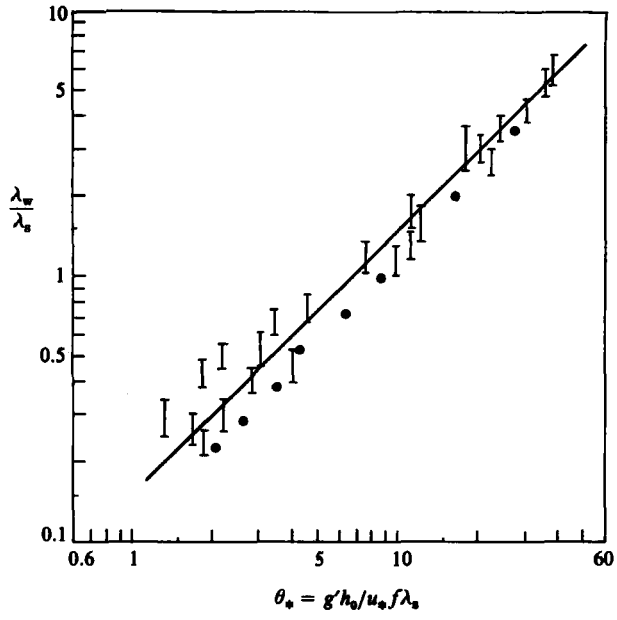

FIGURE 8. The variation of λ_w/λ_s with θ_*, where λ_w is the average size of the frontal cyclones or anticyclones. The dots are the average of the data taken from NM1.

5.4. *Drift velocity of the baroclinic waves*

In the experiments of Saunders (1973), Griffiths & Linden (1981*a*) besides dye they also used streak photography of surface particles to reveal the structure of the circular baroclinic waves. In their experiments the camera was set in the rotating frame of the turntable, and their streak photographs showed the circular structure of the waves very clearly since the waves had only a small wave velocity. This is clearly shown on figure 2 of Saunders' experiments, where after the waves were formed they remained almost stationary. In the present study the camera, when set in the rotating frame of the turntable, could not record the circular structure of the waves because the waves had considerable drift velocity in the direction of the applied stress and the streak photographs showed only a wave pattern (see figure 11*a*). To compensate for this, we set the camera (while in the rotating frame of the turntable) to rotate close to the mean speed of the waves in order to reveal their structure more clearly (for example see figures 9 and 11).

In our experiments when baroclinic waves first appeared at the front, they had their lowest drift velocity in the direction of the applied stress. As the neighbouring waves combined and larger waves were generated, the drift velocity of the waves increased. When the waves reached their equilibrium size λ_w they also reached their maximum speed u_w. In figure 9 we show photographs taken with a rotating camera which demonstrates the drift velocity of these travelling frontal waves. From photographs like these, we measured the speed of the waves by measuring their distance from a fixed point on the tank in a number of experiments. The measured values of u_w were non-dimensionalized by u_* and plotted against the value of θ_*, as shown on figure 10. This plot indicates that the values of u_w/u_* are independent of the values of θ_*, so that

$$\frac{u_w}{u_*} \approx 5. \tag{14}$$

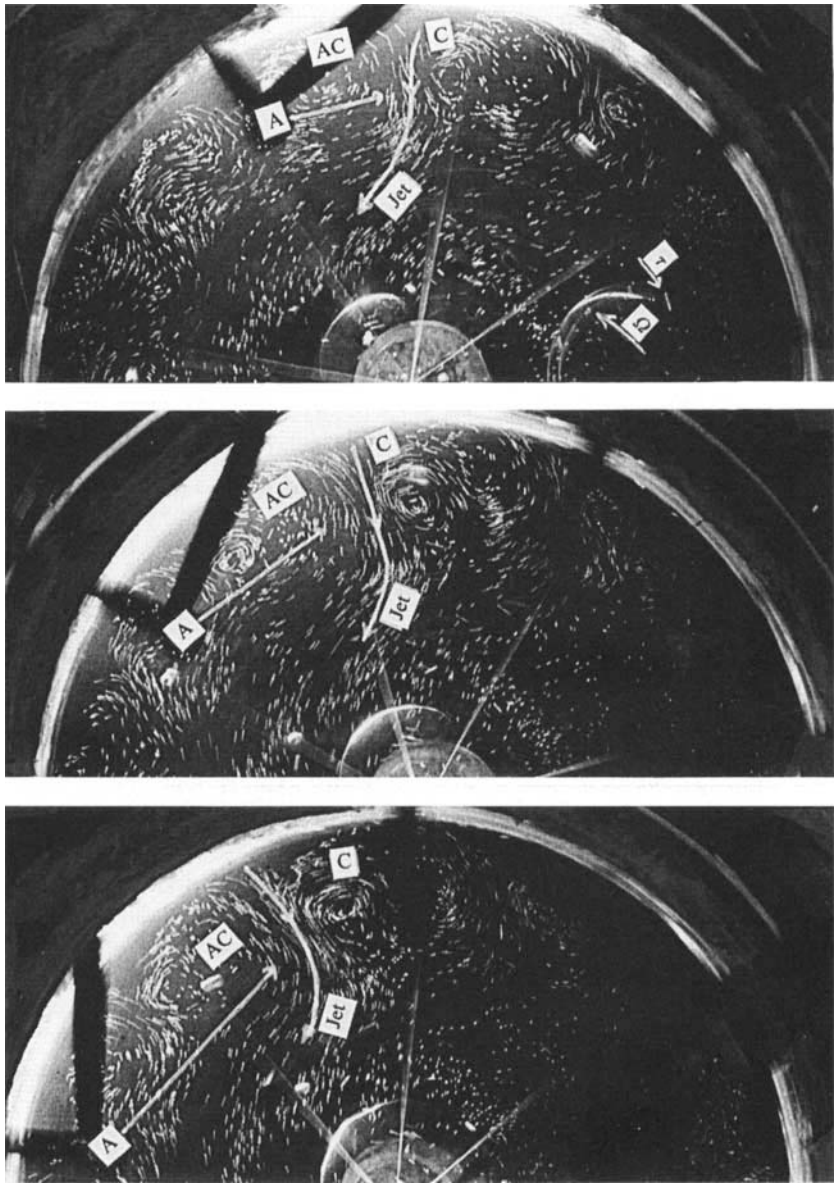

FIGURE 9. A set of streak photographs with the camera rotating with a speed close to that of the waves showing the drift velocity of the frontal waves. For parameter values see figure 7. In (*a*) we have marked a counter-rotating frontal cyclone (C)–anticyclone (AC) pair and the resultant outward jet. (*b*), taken one rotation period later, shows that the pattern has drifted in the direction of the applied stress. (*c*) was taken one rotation period later than (*b*) and shows the further drift of the pattern. The speed of the waves in this experiment was about $u_w \approx 1.7$ cm s^{-1}. The directions of Ω and the applied stress are indicated in (*a*).

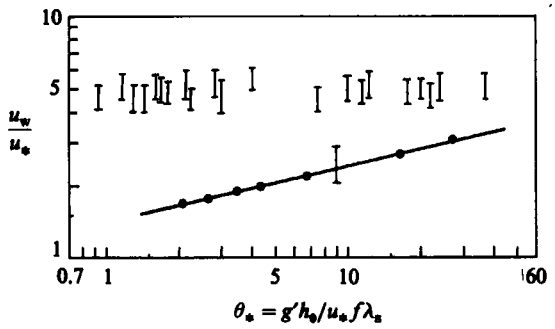

FIGURE 10. The variation of u_w/u_* with θ_*, where u_w is the drift velocity of the frontal waves. The bottom curve is the average of the data taken from NM1.

Based on the mean velocity of the top layer (see §2), (14) becomes

$$u_w = 0.5U = 0.37U_p, \tag{15}$$

indicating that the final speed of the frontal waves is about half the mean velocity of the top layer. This is consistent with the results of Phillips (1954) and Pedlosky (1979, p. 485) from which we estimate that the range of values of u_w/U should be from 0.45 to 0.55 for the depth ratios considered in this study.

In figure 10 we also show the average of the data taken from NM1's plots of u_w/u_* versus θ_*. The much lower values of u_w/u_* in the experiments of NM1 when compared with those of present study indicate that the strong blocking effects of the ridge caused the average speed of the upstream waves to be reduced to almost half that without the ridge. The magnitude of this effect presumably depends on the size of the bottom topographic feature.

6. The generation of plumes, jets and pinched-off cyclones

We have already discussed in NM1 how horizontal plumes containing bottom fluid can be generated by the presence of bottom topography and how they can transport that fluid far offshore. These plumes were generated at the ridge and downstream of it in the form of standing waves to produce permanent upwelling maxima. In the present study we observed similar plumes containing bottom fluid; however they were not permanent nor stationary features and they could occur anywhere around the edge of the upwelled front (see figure 11) as they drifted in the direction of the applied stress. These plumes were a result of the large-amplitude baroclinic instability of the upwelling front, which created a wave trough which penetrated with considerable speed into the lighter fluid, i.e. towards the tank centre (see figure 11 *a*, *b*; location A and B). Here figure 11 (*a*) was taken in the rotating frame of the turntable, while in figure 11 (*b–d*) the camera was rotating with a speed almost equal to that of frontal waves, in order to reveal their vortex-like structure. The generation, development and penetration of one of these plumes can be seen in figure 11 (*b*), where as it propagates outward, the head of the wave narrows and finally a cyclone pinches-off from the head of the plume (see figure 11 *b–d*; location B). On the other hand, in figure 11 (*a*), at location A, the propagating plume (P) is well developed and a cyclone has already pinched-off from its head (figure 11 *b* PC). As time progresses

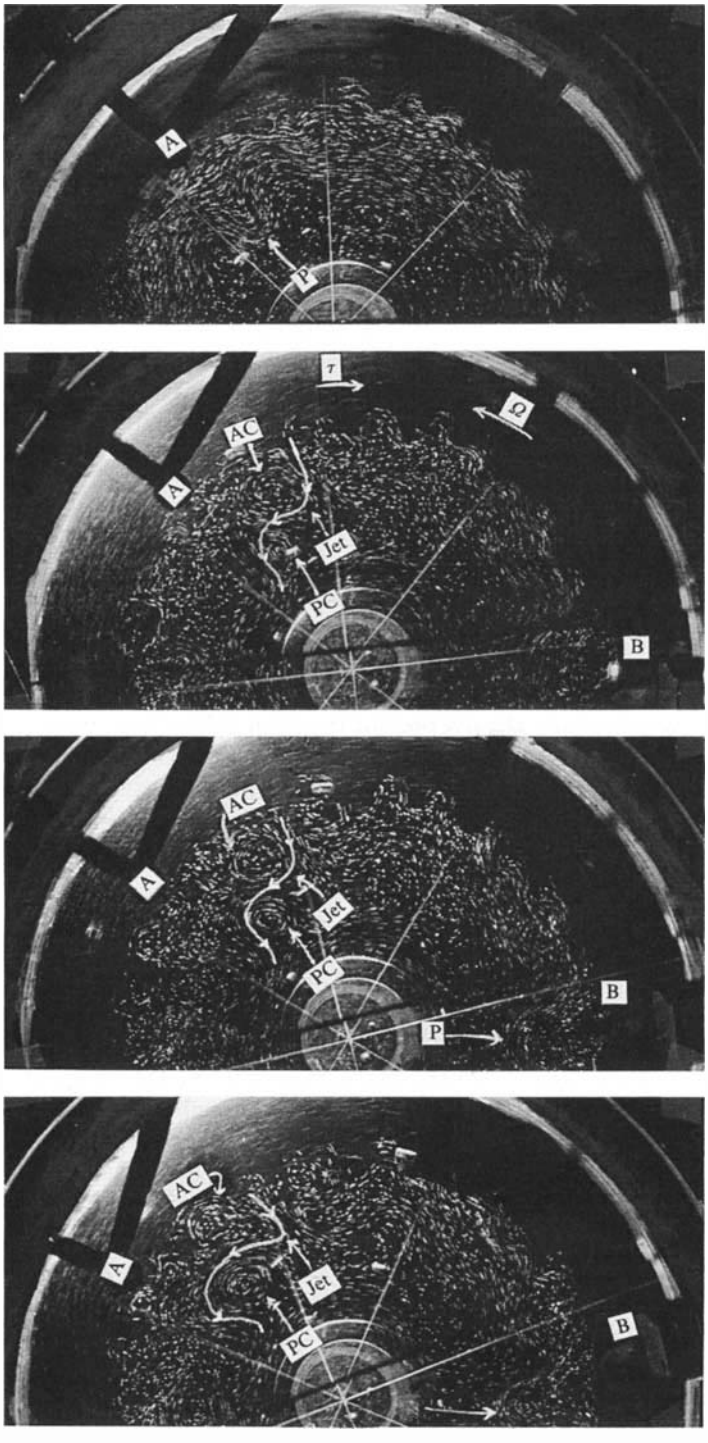

FIGURE 11. For caption see facing page.

its diameter increases to a value considerably greater than that of other frontal waves (see figure 11(*d*) location A). Such a phenomenon was also observed in experiments of NM1, upstream of the bottom topography. This growth could be due to the necessary increase in size associated with the spin-down of the eddy and/or to a gain in vorticity by interaction with other eddies close to it. During this process the size of the frontal anticyclone decreased. This growth of the wave amplitude to pinch-off of an eddy was observed to occur always at low values of $\theta_*(\approx 2)$, that is high values of $U_* f$. More details of this interaction are demonstrated in figure 12 using both streak photography and dye injection into the upwelled fluid, for an experiment with a low value of θ_*, where the pinched-off cyclones and the resulting offshore jets are much more energetic than those of figure 3, where the value of θ_* is larger (≈ 6).

In figure 11, downstream A, there is a frontal anticyclone (AC), the structure of which is very well revealed in figure 11(*b*). The interaction of this anticyclone with the neighbouring pinched-off cyclone leads to generation of an outward meandering jet which carries filaments of bottom fluid a considerable distance outward (i.e. toward the centre of the tank). Similar filaments of bottom fluid, in the form of outward meandering jets, are seen also in many satellite IR images of the ocean surface.

It is evident that counter-rotating vortices, such as those of figures 11 and 12, can produce offshore jets of bottom water and appear to be responsible for transportation of this coastal water far offshore; a mechanism which could have its counterpart in natural flows.

As a result of the observations and discussion presented above it seems appropriate to extent our interpretation of the results presented in NM1. In particular the presence of the ridge in the experiments of NM1 produced a jet-like plume at the ridge, which extended a considerable distance downstream in form of large standing waves, with trapped cyclones with them (figure 13). At low values of θ_*, the first and the largest of the standing waves was formed so close to the ridge that it interacted with the flow over it to create a large trapped anticyclone (TAC) just downstream of the ridge, as seen in figure 13. In this case also the crest of the standing wave propagated outward and after few rotation periods a cyclone pinched-off from the crest of this standing wave. This cyclone then interacted with the TAC to produce an outward meandering jet, as indicated on figure 13. Such a phenomenon has been reported by Mooers & Robinson (1984), in their observations of coastal-upwelling circulation downstream of the Mendocino Ridge, off the west coast of California; while

---

FIGURE 11. A set of streak photographs with a 0.5 s time exposure. For parameter values see figure 2. (*a*) was taken in the rotating frame of the turntable, and shows a propagated outward plume (P) containing bottom fluid (marked as P at location A). (*b*) was taken one rotating period later. In this case the camera was rotating with the waves in order to reveal their structure. Notice the pinched-off cyclone (PC) which has come from the head of the propagating plume, its interaction with the frontal anticyclone (AC) and the resultant outward meandering jet are indicated. In this photograph at location B a new plume is ready to grow in amplitude. In (*c*), taken one rotation period later, the PC has grown and drifted in the direction of the applied stress. The head of the plume at B has propagated farther outward. (*d*) was taken one rotation period later. The size of the PC has grown to a large value (about 3 to 4 times greater than that of the frontal waves), while the size of the AC is considerably reduced, and the whole pattern has drifted in the direction of the applied stress. A new cyclone is about to pinch-off from the head of the plume at B to repeat the processes that occurred at location A. Directions of Ω and applied stress τ are indicated in (*b*).

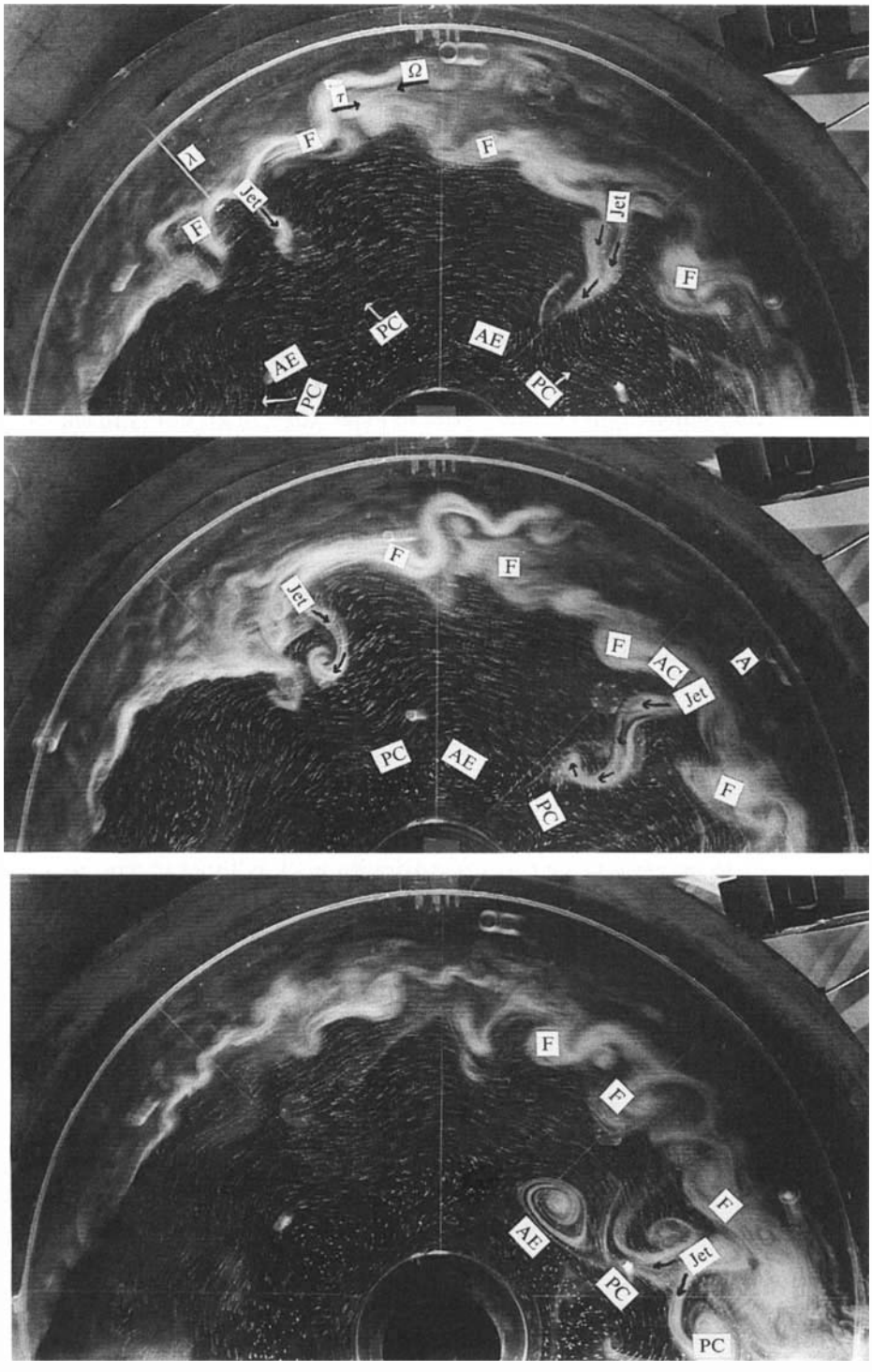

FIGURE 12. For caption see facing page.

observation of a pinch-off cyclone was reported by Rienecker *et al.* (1985) at the same location.

It appears from the present study and NM1 that the pinch-off process described above occurs when $\theta_* \leqslant 6$, and that outward-moving filaments or turbulent jets may be generated by interaction between a frontal anticyclone and a nearby pinched-off cyclone. These jets can carry bottom fluid a considerable distance outward, and could be the major reason for the observation of such filaments in many satellite images.

7. Summary and conclusions

We have produced a model of coastal upwelling on a sloping bottom in the absence of bottom topographic features and coastline pertubations. We have found that θ_* is a suitable parameter for determining many aspects of the coastal-upwelling circulation. For example we find that the front migration rate $u_f/u_* \sim \theta_*^{\frac{1}{2}}$; that the size of the frontal waves $\lambda_w/\lambda_s \sim \theta_*$ while such waves appear when the front is a distance λ_i from the coast, where the $\lambda_i/\lambda_s \sim \theta_*^{\frac{1}{2}}$. These results indicate the importance of the single non-dimensional parameter θ_* in understanding the dynamics of coastal upwelling. Interestingly θ_* is a combination of two important and well-known parameters in geophysical fluid dynamics and oceanography, the Richardson number $Ri_* = g'h_0/u_*^2$ and the Rossby deformation radius $(g'h_0)/f\lambda_0$ so that $\theta_* = Ri_*^{\frac{1}{2}}\theta$. We found also that the drift velocity of the baroclinic frontal waves is about $u_w \approx 0.5U$, in the direction of the applied stress, where U is the mean fluid velocity at the front.

Plumes containing bottom fluid were observed to propagate outward when $\theta_* \leqslant 6$. A cyclone containing bottom fluid is then pinched-off from the head of these plumes to generate isolated cyclonic eddies which, at a later time, grow to a size considerably greater than that of the frontal waves. These pinched-off cyclones then interact with one of the frontal anticyclone eddies or (waves) to produce an outward meandering jet which may carry parcels of bottom fluid from the mean location of the front. These jets and filaments are seen in many satellite images. Unlike the stationary plumes observed at and downstream of bottom topography (figure 13), the plumes of the present study may occur anywhere around the upwelled front and propagate away from the coast and in the direction of the applied stress. Note that for the values of $\theta_* > 6$, although baroclinic waves appear at the front, no pinched-off cyclones were observed.

In some of our experiments beside particles at the interface, the top layer was also dyed by fluorescein (figure 14). Soon after the stress was applied to the top surface

---

FIGURE 12. A set of combined dye and streak photographs with 0.5 s time exposure and with parameter values of $\Omega = 2.47$ rad s^{-1}, $\Delta\Omega = 0.18$ rad s^{-1}, $h_0 = 2.6$ cm, $\delta\rho_0 = 0.026$ g cm^{-3}, $\lambda_s \approx 17.4$ cm, $u_* \approx 0.35$ cm s^{-1} and $\theta_* \approx 2.2$. (*a*) was taken after 200 rotation periods, showing a number of pinched-off cyclones (PC). Notice of offshore anticyclonic eddies (AE) which are produced between the pinched-off cyclonic eddies. This photograph clearly shows the offshore transport of the dyed bottom upwelled water at the location of the pinched-off cyclones. In this figure some of the frontal waves are indicated by F. Unlike figure 11, here the circular form of the waves is not revealed by the particle streaks because the camera was not rotating with the waves, so that the dye must be used to reveal the form of the frontal and offshore waves. (*b*), taken 2 rotation periods after (*a*), shows a meandering offshore jet at A, which is associated with the indicated frontal and offshore eddies (PC, AC). (*c*) was taken 11 rotation periods after (*b*), and shows the continued evolution of the jets of (*b*). The circular form of the pinched-off cyclones and offshore anticyclones is clearly outlined by the dye in this photograph.

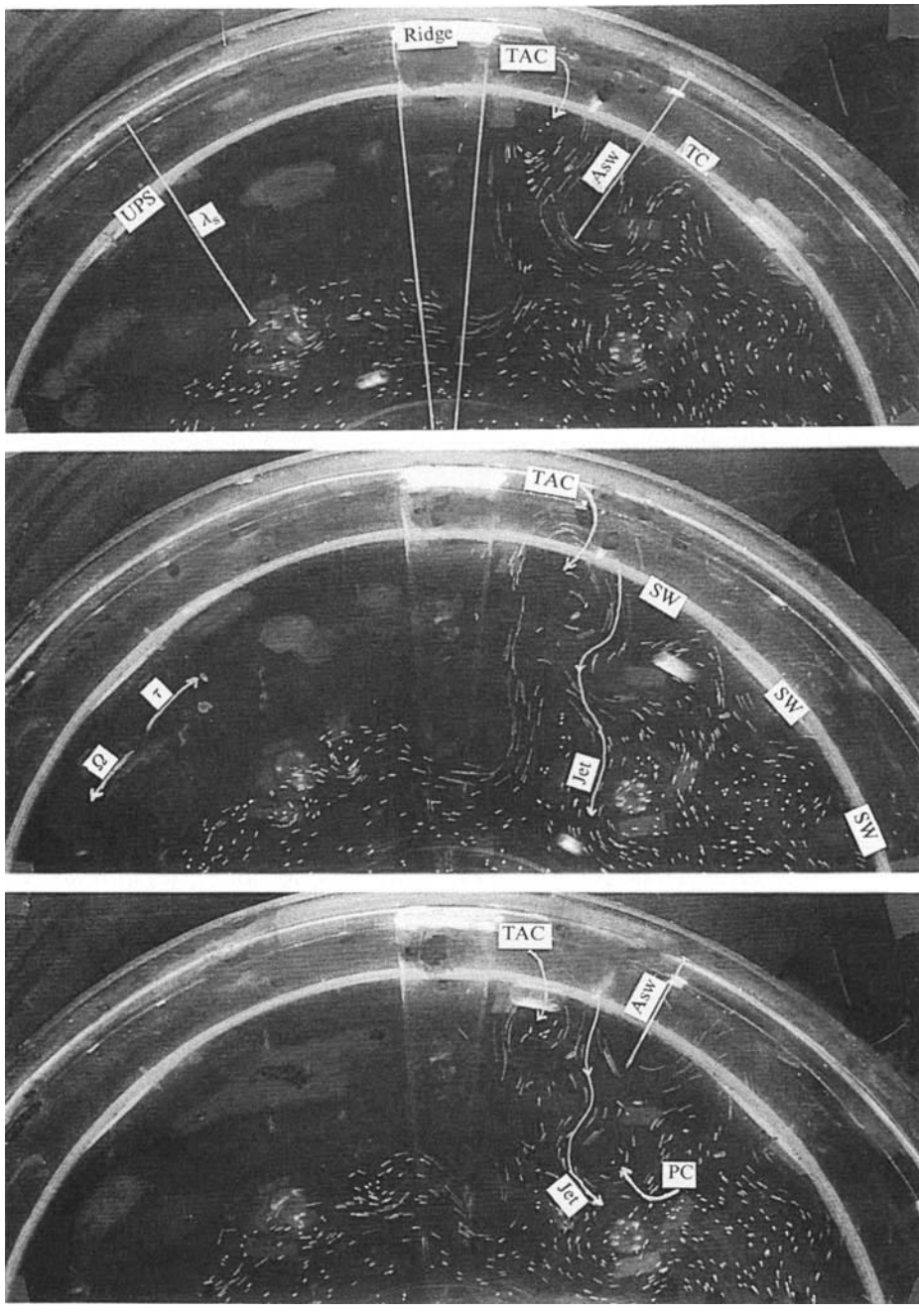

FIGURE 13. A set of streak photographs taken from the experiments of NM1 (their figure 18) with, $f = 5.82$ rad s^{-1}, $h_0 = 2.6$ cm, $g' = 19.62$ cm s^{-1}, $\Delta\Omega = 0.125$ rad s^{-1}, $u_* = 0.24$ cm s^{-1}, $\lambda_s = 17.67$ cm and $\theta_* = 2.03$. In these photographs the position of the ridge is shown on (*a*), while the direction of turntable rotation Ω, and the applied stress τ are indicated in (*b*). In (*a*) the amplitude of the downstream standing wave (A_{sw}) is large and the trapped cyclone (TC) within this wave interacts with the trapped anticyclone (TAC). UPS stands for upstream. (*b*) Taken two rotation periods later, shows that the standing wave is about to release the trapped cyclone from its crest. This has resulted in the generation of the indicated outward meandering jet. The positions of the downstream standing waves are denoted by SW. (*c*) taken two rotation periods later than (*b*), shows that the TC has now pinched-off PC but is still interacting with the TAC, and the resulting meandering outward jet can still be seen. After losing the cyclone, the amplitude of the first standing wave has returned to its original value.

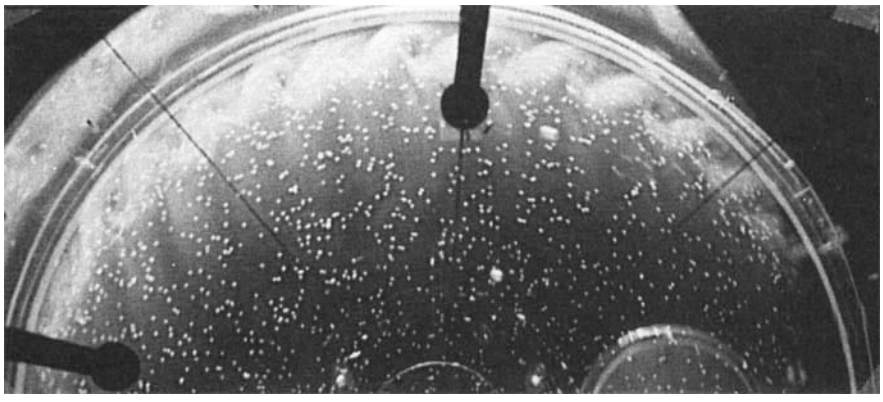

FIGURE 14. A streak photograph taken soon after the stress was applied to the top surface from an experiment with value of $\theta_* \approx 6$. The appearance of Kelvin–Helmholtz billows is revealed clearly by fluorescien dye, while the particles at the interface show no indication of baroclinic-wave-type instabilities.

a Kelvin–Helmholtz type of instability appeared at the density interface around the outer edge of the tank. This observation agrees with that of Griffiths & Linden (1982) who were the first to report experiments in which K–H billows appeared almost immediately at a density front before the appearance of the baroclinic waves.

The authors wish to thank Mr Casey De Vries for assistance in the laboratory and for bringing the experimental apparatus to working condition and Mrs Jacquette Givens for typing this manuscript. Financial support was from the National Science Foundation, Grant No. OCE-8214549.

REFERENCES

BERNSTEIN, R. L., BREAKER, L. & WHIRTNER, R. 1977 California current eddy formation: ship, air and satellite results. *Science* **195**, 353–359.

BREAKER, C. L. & MOOERS, C. N. K. 1985 Oceanic variability off the central California coast. *Prog. Oceanogr.* (submitted).

BRINK, K. H., JONES, B. H., VAN LEER, J. C., MOOERS, C. N. K., STUART, D. W., STEVENSON, M. R., DUGDALE, R. C. & HEBURN, G. W. 1981 Physical and biological structure and variability in an upwelling center off Peru near 15° S during March, 1977. In *Coastal Upwelling* (ed. F. A. Richards), pp. 473–495. AGU.

BRINK, K. H., HALPERN, D. & SMITH, R. L. 1980 Circulation in the Peruvian upwelling system near 15 °S. *J. Geophys. Res.* **85**, 4036–4048.

CHIA, F. R., GRIFFITHS, R. W. & LINDEN, P. F. 1982 Laboratory experiments on fronts. Part II. The formation of cyclonic eddies at upwelling fronts. *Geophys. Astrophys. Fluid Dyn.* **19**, 189–206.

DOUGLAS, R. A., HIDE, R. & MASON, P. J. 1972 An investigation of the structure of baroclinic waves using three-level photography. *Q. J. R. Met. Soc.* **98**, 247–263.

EADY, E. T. 1949 Long waves and cyclone waves. *Tellus* **1**, 35–52.

FLAMENT, P., ARMI, L. & WASHBURN, L. 1985 The evolving structure of an upwelling filament. *J. Geophys. Res.* **90**, 11783–11798.

GRIFFITHS, R. W. & LINDEN, P. F. 1981*a* The stability of vortices in a rotating, stratified fluid. *J. Fluid Mech.* **105**, 283–316.

GRIFFITHS, R. W. & LINDEN, P. F. 1981*b* The stability of buoyancy driven coastal currents. *Dyn. Atmos. Oceans* **5**, 281–306.

GRIFFITHS, R. W. & LINDEN, P. F. 1982 Laboratory experiments on fronts. Part I. Density driven boundary currents. *Geophys. Astrophys. Fluid Dyn.* **19**, 159–187.

HALPERN, D. 1976 Structure of a coastal upwelling event observed off Oregon during July 1973. *Deep Sea Res.* **23**, 495–508.

HALPERN, D. 1977 Description of wind and of upper ocean currents and temperature variation on the Continental Shelf off Northwest Africa during March and April 1977. *J. Phys. Oceanogr.* **7**, 422–430.

HART, J. E. 1972 A laboratory study of baroclinic instability. *Geophys. Fluid Dyn.* **3**, 181–209.

HART, J. E. 1980 An experimental study of nonlinear baroclinic instability and mode selection in a large basin. *Dyn. Atmos. Oceans* **4**, 115–135.

HIDE, R. 1971 Laboratory experiments of free thermal convection in a rotating fluid subject to a horizontal temperature gradient and their relation to the theory of the global *atmospheric* circulation. *The Global Circulation of the Atmosphere*, pp. 196–221. Roy. Meteror. Soc. and Amer. Meteror. Soc.

HUYER, A., SMITH, R. L. & HICKEY, B. M. 1984. Observation of a warm-core eddy off Oregon, January to March, 1978. *Deep-Sea Res.* **31**, 97–117.

KANTHA, L. H., PHILLIPS, O. M. & AZAD R. S. 1977 On turbulent entrainment at a stable density interface. *J. Fluid Mech.* **79**, 753–768.

KILLWORTH, P. D., PALDOR, N. & STREN, M. 1984 Wave propagation and growth on a surface front in a two-layer geostrophic current. *J. Mar. Res.* **42**, 761–785.

LINDEN, P. F. & VAN HEIJST, G. J. F. 1984 Two-layer spin up and frontogenesis. *J. Fluid Mech.* **143**, 69–94.

MAXWORTHY, T. 1977 Topographic effects in rapidly-rotating fluids: flow over a transverse ridge. *Z. angew. Math. Phys.* **28**, 853–864.

MAXWORTHY, T. & NARIMOUSA, S. 1985 Experiments and observations on the effects of bottom topography on coastal upwelling. *Symp. on Vertical Motion in the Equatorial Upper Ocean and its Effects upon Living Resources and the Atmosphere, 6–10 May 1985, Paris.*

MOOERS, C. N. K., COLLINS, C. A. & SMITH, R. S. 1976 The dynamics structure of the frontal zone in the coastal upwelling region off Oregon. *J. Phys. Oceanogr.* **6**, 3–21.

MOOERS, C. N. K. & ROBINSON, A. R. 1984 Turbulent jets and eddies in the California current and inferred cross-shore transports. *Science* **223**, 51–53.

NARIMOUSA, S., LONG, R. R. & KITAIGORODSKII, S. A. 1985 Entrainment due to turbulent shear flow at the interface of a stably stratified fluid. *Tellus* **38A**, 76–87.

NARIMOUSA, S. & MAXWORTHY, T. 1985 Two-layer model of shear-driven coastal upwelling in the presence of bottom topography. *J. Fluid Mech.* **159**, 503–531.

NARIMOUSA, S. & MAXWORTHY, T. 1986*a* Laboratory modeling of coastal upwelling. *Transactions, American Geophysical Union EOS*, 67, No. 1, 2–3.

NARIMOUSA, S. & MAXWORTHY, T. 1986*b* Effect of a discontinuous surface stress on a model of coastal upwelling. *J. Phys. Oceanogr.* (in press).

PEDLOSKY, J. 1979 *Geophysical Fluid dynamics.* Springer.

PHILLIPS, N. A. 1954 Energy transformations and meridional circulations associated with simple baroclinic waves in a two-level, quasi-geostrophic model. *Tellus* **6**, 273–286.

PRELLER, R. & O'BRIEN, J. J. 1980 The influence of bottom topography on upwelling off Peru. *J. Phys. Oceanogr.* **10**, 1377–1398.

RIENCKER, M. M., MOOERS, C. N. K., HAGAN, D. E. & ROBINSON, A. R. 1985 A cool anomaly off Northern California: an investigation using IR imagery and *in situ* data. *J. Geophys. Res.* **90**, 4807–4818.

SIMPSON, J. J., DICKEY, T. D. & KOBLINSKY, C. J. 1984 An offshore eddy in the California current system. *Prog. Oceanogr.* **13**, 5–49.

SAUNDERS, P. M. 1973 The instability of a baroclinic vortex. *J. Phys. Oceanogr.* **3**, 61–65.